Yu *et al. Advances in Aerodynamics* (2023) 5:21
https://doi.org/10.1186/s42774-023-00152-2

Advances in Aerodynamics

RESEARCH Open Access

Predicting wing-pylon-nacelle configuration flutter characteristics using adaptive continuation method

Qijing Yu[1,2*], M. Damodaran[3] and B. C. Khoo[3,4]

*Correspondence:
yuqj@ouchn.edu.cn

[1] Department of Mechanical Engineering, The Open University of China, Beijing 100039, China
[2] Engineering Research Center of Integration and Application of Digital Learning Technology, Ministry of Education, Beijing 100039, China
[3] Temasek Laboratories, National University of Singapore, Singapore 117411, Singapore
[4] Department of Mechanical Engineering, National University of Singapore, Singapore 117575, Singapore

Abstract

In this study, the aeroelastic response of a wing-pylon-nacelle system in subsonic and low supersonic flow regimes is analyzed using the continuation method in conjunction with an adaptive step size control algorithm. Idealizing the pylon and nacelle as a point mass, the computed effects of a standard structural analysis of the wing together with the pylon and nacelle are compared with those of a clean wing to build a reduced-order model for analysis. The aerodynamic forces relating to different reduced frequencies are assessed using the Doublet Lattice Method (DLM) in the subsonic flow regime and supersonic lifting surface theory relying on the unsteady linearized small-disturbance potential flow model in the low supersonic flow regime. The Rational Function Approximation (RFA) method is then utilized for the state-space formulation of the system equations, appended with the continuation method for flutter prediction. Thereafter, the linearized aeroelastic equations are resolved using the continuation method with adaptive step size, the results of which are matched with those obtained from the traditional *p-k* method to emphasize that the continuation method exhibits a distinct advantage in achieving better accuracy in estimating the flutter speed and identifying the "mode switching" phenomenon.

Keywords: Aeroelasticity, Continuation method with adaptive step-size, Flutter

1 Introduction

Flutter is an oscillatory motion resulting from the interaction between aerodynamic forces and structural vibrations which can result in a loss of control or serious damage to the aircraft. For these reasons, flutter characteristics of aircraft structures in fluid flow are analyzed for mitigating the consequences of flutter. Most instants of flutter or limit cycle oscillation (LCO) encountered in aircraft flight can be attributed to the presence of multiple structural nonlinearities present in control surface free-plays, underwing or wingtip attached external stores, hysteresis, and cubic stiffness of materials as outlined in Woolston et al. [1], Laurenson and Trn [2], Lee [3], Yang and Zhao [4] and Lee and Tron [5]. Among the various types of structural nonlinearities, an external store could cause a significant effect on the aeroelastic responses of an aircraft wing. For example, the flight test data of Laurenson and Trn [2] and the numerical simulations of Chen et al. [6] have

shown that the effect of external stores on the flutter boundaries for F16A fighter aircraft with missiles fitted on the wings can be significant for both typical LCO and non-typical LCO cases. Wing-mounted engine nacelle treated as structural nonlinearity on the flutter and LCO characteristics of the configuration are worthy of an investigation and have been investigated in a number of studies. Försching et al. [7] investigated the flutter behaviour of a binary wing-with-engine nacelle system using the inviscid incompressible flow model for a variety of systematic parameter variations. Arizono et al. [8] computed transonic flutter of a wing-pylon-nacelle configuration using a thin-layer approximation compressible Navier–Stokes flow model to show the effect of viscosity on the flow on its flutter boundary. Wang et al. [9] analyzed an aeroelastic model of the wing/engine system of a large commercial aircraft by considering the effect of engine inertial force and thrust, static aeroelastic deformation of the wing structure, and load distributions on the aeroelastic response. Neuert et al. [10] investigated the aeroelastic behaviour of a wing with a bypass ratio engine and high-lift devices using a reduced-order model where the results indicated heave instabilities can occur at strongly negative angles of attack. The present study stems from the authors' earlier work, Yu et al. [11] on the aeroelastic analysis of a wing-pylon-nacelle configuration based on the geometry of the JAXA Standard Wing Model (JSM) defined for the NASA high lift prediction workshop outlined in Ref. [12] for operations at both subsonic and low supersonic flight regimes. The structural characteristics of the clean wing (defined here as the JSM_*c* model) and the wing-pylon-nacelle-engine model (defined here as the JSM_*enp* model) are analyzed using *NX Nastran* [13] Finite Element Method (FEM). The Doublet-Lattice Method (DLM) based on the Prandtl-Glauert transformation for compressible subsonic flow outlined in Albano and Rodden [14] and ZONA51 outlined in Liu et al. [15] which is based on the supersonic lifting surface theory developed from the unsteady linearized small disturbance potential flow equation for the low end of the supersonic flow regime are used to estimate the aerodynamic loads for different reduced frequencies. In this study, the innovative adaptive step size control algorithm developed and applied by the authors in Yu et al. [16, 17] is combined with the classical Continuation Method (CM) outlined in Trajkovic et al. [18] to analyze the flutter characteristics of this configuration by solving the linearized aeroelastic equations in the frequency domain very efficiently while maintaining improved accuracy compared with the traditional eigenvalue analysis and the *p-k* method.

2 Description of wing-pylon-nacelle configuration

The wing-pylon-nacelle configuration considered in this study includes an underwing single-engine mass attached to the clean JSM wing model, the properties of which are defined in Yokokawa et al. [19]. The effect of the engine mass is considered as a lumped mass located on the center of gravity (CG) of the engine nacelle and pylon mount which is assumed to be located at 60% of the distance between the inlet and the end of the pylon nacelle as reported in Chai et al. [20]. The original JSM wing is approximated with two sections of plate elements to form the FEM model shown in Fig. 1, which also shows the location of the engine point mass, the mean aerodynamic chord of the wing, and the change in CG location due to the engine mass. As the specifications of the JSM are similar to those of the Boeing B787 series, the engine mass for this study is based on the GEnX engine for the Boeing B787,

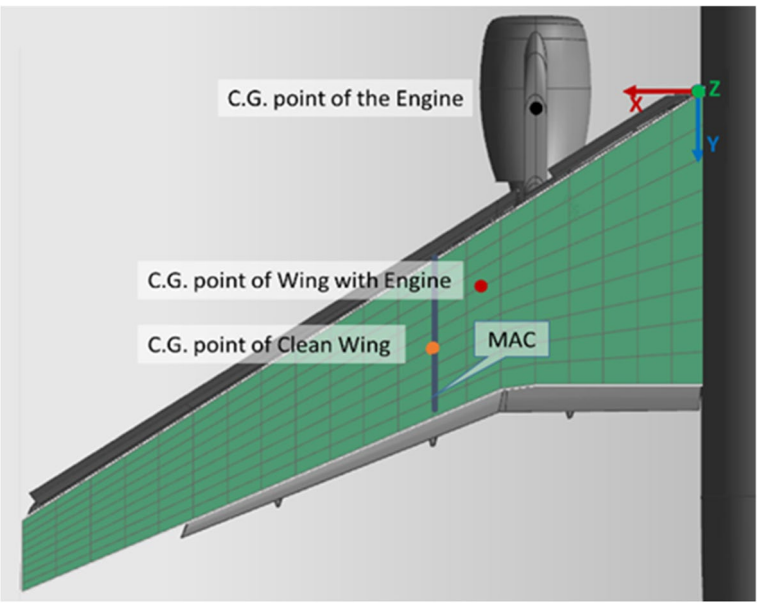

Fig. 1 Simplified JSM wing-pylon-nacelle (JSM_*enp*) model

which has an original dry mass of 5816 kg. As the estimated length ratio between real aircraft and the model is 10:1, the scaled point mass of 5.816 kg is assumed to be acting at the estimated center of gravity of the engine nacelle and pylon shown in Fig. 1. The wing in both JSM_*c* and JSM_*enp* models has a semi-span of 2.3 m, a mean aerodynamic chord of 0.5292 m, a leading-edge wing sweep angle of 33° and a wing taper ratio of 0.333. The moduli of elasticity in the longitudinal direction (E_1) and lateral direction (E_2) are 3.1511 GPa and 0.4162 GPa respectively. The Poisson's ratio (υ) is 0.31, the shear modulus (G) is 0.4392 GPa and the density (ρ) of the material used in the wing is 381.98 kg/m^3. Both the choice of plate element type and the mesh density are critical for fast analysis by efficient FEM. The mesh dependency test is conducted first with results shown in Fig. 2 by considering the variation of a selected parameter of interest with mesh density to assess the impact of mesh density on the computed results. The parameter of choice in this study is the frequency of the first torsion mode of the JSM model computed using the SOL 103 solver in *NX Nastran*. It can be seen from Fig. 2 that as the number of plate elements, i.e., CQUAD4, increases to 180 and beyond, the effect of the mesh density on the computed value of the parameter becomes almost invariant. A similar mesh convergence study has been used to assess the impact of six different types of 2D plate elements as shown in Fig. 3, which shows that when the mesh density is kept fixed, only small discrepancies (less than 5%) can be observed in terms of mesh convergence. The FEM model of the JSM wing used in this study consists of 10 grid points along the chord-wise direction and 21 points along the span-wise direction, leading to 210 grid points and 180 plate elements (CQUAD4) in total.

3 Computational aeroelastic modeling

3.1 Real modal analysis and formulation of reduced order model

The structural equations of motion resulting from a FEM model of a three-dimensional wing without external loading are given by:

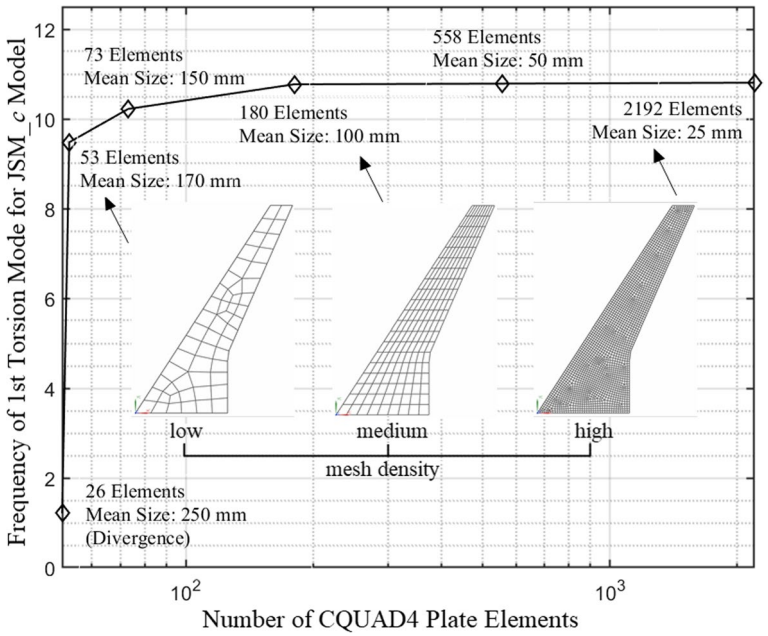

Fig. 2 Independency check for the mesh size

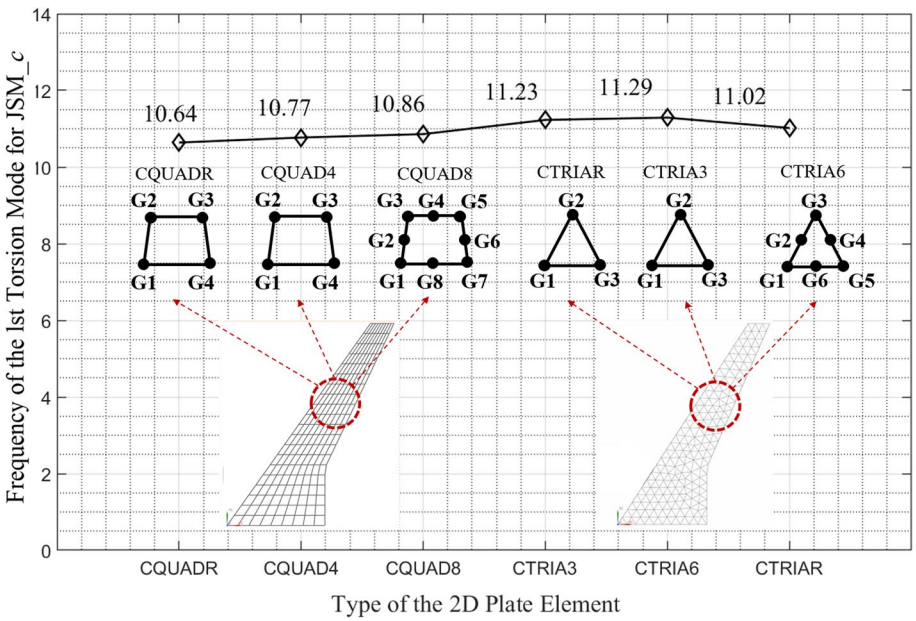

Fig. 3 Independency check for the element type used in FEM

$$\boldsymbol{M}\ddot{\boldsymbol{q}} + \boldsymbol{K}\boldsymbol{q} = 0, \tag{1}$$

where $\boldsymbol{M}, \boldsymbol{K} \in \mathbb{R}^{n\times n}$ are the mass and stiffness matrices, and $\boldsymbol{q} \in \mathbb{R}^{n\times 1}$ is the displacement vector. For this study, the structural damping is ignored. For more efficient computations, a reduced order model could be achieved by using a Model Order Reduction (MOR) technique. This study uses the method of real modal analysis, in which a number

of fundamental natural mode shapes, i.e., $\phi_1 - \phi_m$, of the full-model are selected by solving the eigenvalue equation, i.e.,

$$(\boldsymbol{K} - \lambda_i \boldsymbol{M})\{\phi_i\} = 0, \tag{2}$$

where $\lambda_i = \omega_i^2$, ω_i is the i^{th} natural frequency, and eigenvector $\phi_i \in \mathbb{R}^{m\times 1}$ is the i^{th} mode shape. Equation (2) is a set of homogeneous algebraic equations which are solved for the real eigenvalues for extracting the elastic modes by using the Lanczos method, outlined in Komzsik et al. [21] and embodied in the SOL 103 solver in *NX Nastran.* All mode shapes are orthogonal to both the mass and the stiffness matrices, i.e.,

$$\phi_i^T \boldsymbol{M} \phi_j = \begin{cases} 0 \, for \; i \neq j \\ m_i \, for \; i = j \end{cases}, \tag{3a}$$

$$\phi_i^T \boldsymbol{K} \phi_j = \begin{cases} 0 \, for \; i \neq j \\ K_i \, for \; i = j \end{cases}, \tag{3b}$$

Hence the reduced order mass and stiffness matrices, i.e., $\boldsymbol{M_r}$ and $\boldsymbol{K_r}$, can be derived on the basis of the orthogonality property:

$$\boldsymbol{M_r} = \boldsymbol{\Phi}^T \boldsymbol{M} \boldsymbol{\Phi}, \tag{4a}$$

$$\boldsymbol{K_r} = \boldsymbol{\Phi}^T \boldsymbol{K} \boldsymbol{\Phi}, \tag{4b}$$

$$\boldsymbol{q} = \boldsymbol{\Phi} \boldsymbol{\eta}, \tag{4c}$$

where $\boldsymbol{\Phi} = [\phi_1, \phi_2, \ldots, \phi_m] \in \mathbb{R}^{n\times m}$ is the modal matrix, and $\boldsymbol{\eta} \in \mathbb{R}^{m\times 1}$ are the modal coordinates. The reduced order model is thus given by:

$$\boldsymbol{M_r} \ddot{\boldsymbol{\eta}} + \boldsymbol{K_r} \boldsymbol{\eta} = 0. \tag{5}$$

3.2 Aerodynamic solvers

The Doublet Lattice Method is used for modeling aerodynamic loads in the subsonic flow field while the ZONA51 method is used for modeling aerodynamic loads in the low end of the supersonic flow regime, considering their simplicity and versatility. Both DLM and ZONA51 are based on the potential flow theory and solve the steady and unsteady three-dimensional linearized small disturbance potential equation, i.e.,

$$\left(1 - M_{\text{a}}^2\right)\varphi_{xx} + \varphi_{yy} + \varphi_{zz} - \frac{2M_{\text{a}}^2}{V}\varphi_{xt} - \frac{M_{\text{a}}^2}{V^2}\varphi_{tt} = 0, \tag{6}$$

where the M_a is the Mach number in the freestream flow, V is the free stream airspeed and φ is the disturbance velocity potential function of the flow field. The subscripts are the partial derivatives of the potential function φ with respect to the spatial and temporal coordinates. By assuming the structural motion of the wing model to follow the harmonic form for a small deflection and constant amplitude, Eq. (6) can be transformed into an integral equation and solved using the panel method outlined in Erickson [22]. For computational convenience, the aerodynamic configuration used for this study

corresponds to the simplified model shown in Fig. 4. This is constructed by subdividing the JSM wing model into a series of trapezoidal panels under the assumption of a constant pressure over each panel. For each panel, the unknown lifting pressures are assumed to be concentrated uniformly across the one-quarter chord line of each panel. There is one control point per panel, centered spanwise at the three-quarter chord line, to calculate the downwash function. Equation (6) is solved by imposing the Kutta condition to constrain the pressure difference to be zero at the trailing edge of the wing surface and the no normal flow condition on the wing surface.

About 180 panels tied to the 210 uniformly spaced grid points in the spanwise direction from the root to the tip of the wing are used to develop the aerodynamic influence coefficients for assessing the flutter characteristics. The aerodynamic influence coefficient matrix, i.e., $\boldsymbol{A.I.C}(M_a, k)$, which is a function of Mach number M_a and reduced frequency k, can be obtained from the solutions of Eq. (6) which are computed by the SOL 145 solver in *NX Nastran* [13]. By coupling the aerodynamic forces with structural equations, i.e., Eqs. (1) and (5), the full order and reduced order governing equations for the JSM wing can be written as follows, respectively:

$$\boldsymbol{M}\ddot{\boldsymbol{q}} + \boldsymbol{K}\boldsymbol{q} = q_{dyn}\boldsymbol{A.I.C}(M_a, k)\boldsymbol{q}, \tag{7a}$$

$$\boldsymbol{M_r}\ddot{\boldsymbol{\eta}} + \boldsymbol{K_r}\boldsymbol{\eta} = q_{dyn}\boldsymbol{A.I.C_r}(M_a, k)\boldsymbol{\eta}, \tag{7b}$$

where $q_{dyn} = \frac{1}{2}\rho V^2$ is the dynamic pressure and $\boldsymbol{A.I.C_r}(M_a, k) = \boldsymbol{\Phi}^T\boldsymbol{A.I.C}(M_a, k)\boldsymbol{\Phi}$. The reference density ρ of air is assumed to be 1.225 kg/m^3, and the Mach number for the subsonic and supersonic regions can be varied in the range 0.1–0.8 and 1.1–1.4, respectively, for which the linear aerodynamic flow model is valid. In addition, the wing is assumed to be in a steady straight and level flight, for which the engine thrust balances the drag, or in an engine-power-off flight for facilitating the flutter analysis.

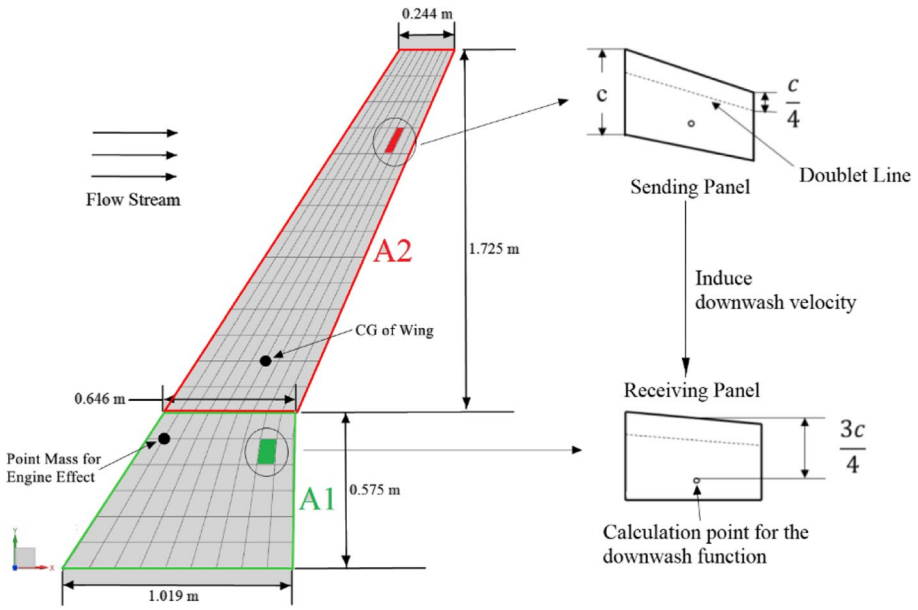

Fig. 4 Simplified aerodynamic model for JSM_*c* and JSM_*enp* models

3.3 The continuation method

The Continuation Method was first introduced for solving algebraic nonlinear problems, in which the solution is treated as an instant of a dynamic problem as shown in Ogrodzki [23]. In the implementation of the classical continuation method, an auxiliary equation is chosen properly to facilitate the solution of the original nonlinear equations. For example, if the original equations to be solved are $\boldsymbol{f}(\boldsymbol{x}) = 0$, then one form of the Continuation Function $\boldsymbol{H}(\boldsymbol{x}, \lambda^*)$ can be constructed as

$$\boldsymbol{H}(\boldsymbol{x}, \lambda^*) = \lambda^* \boldsymbol{f}(\boldsymbol{x}) + (1 - \lambda^*)\boldsymbol{g}(\boldsymbol{x}) = 0, \tag{8}$$

where λ^* is the continuation parameter and $\boldsymbol{g}(\boldsymbol{x})$ is the auxiliary equation. If λ^* is increased from 0 to 1, then $\boldsymbol{H}(\boldsymbol{x}, \lambda^*)$ is continuously deformed from the auxiliary equation $\boldsymbol{g}(\boldsymbol{x}) = 0$, in which solutions could be easily found for the original problem $\boldsymbol{f}(\boldsymbol{x}) = 0$. For the aeroelastic analysis considered in this study, the parameter λ could be considered to be one of the system variables as outlined in Meyer [24]. Numerous methods exist for formulating and solving the continuation function. The approach for using the CM for solving a set of nonlinear equations consists of the formulation of the CM function followed by choosing and implementing an efficient solver. The CM consists of two algorithms, namely the *predictor algorithm* which predicts the solutions at the next value of the continuation parameter, and the *corrector algorithm* which uses the intermediate solutions from the predictor algorithm to obtain the final solution at the end of the step and the repeated application of these steps results in path tracking as shown in Fig. 5. The solution $(\widehat{\boldsymbol{x}}_N, \lambda_N^*)$ is first predicted based on the accurate solution $(\boldsymbol{x}_{N-1}, \lambda_{N-1}^*)$ in the previous step, and then λ^* is fixed temporarily at $\lambda^* = \lambda_N^*$ in the corrector phase to let the corrector algorithm converge to the accurate solution $(\boldsymbol{x}_N, \lambda_N^*)$ in the tracking path. In the predictor phase, the tangent vector $\boldsymbol{t} = (\boldsymbol{t}_{\boldsymbol{x}}, \boldsymbol{t}_{\lambda^*})^T$ is used to determine the direction of the tracking path for each step. It can be defined using the pseudo-arclength method as described in Rodrigues et al. [25] based on the idea of computing the tangent vector $\boldsymbol{t}$ for the zero curve of $\boldsymbol{H}(\boldsymbol{x}, \lambda^*)$. It is expressed as follows:

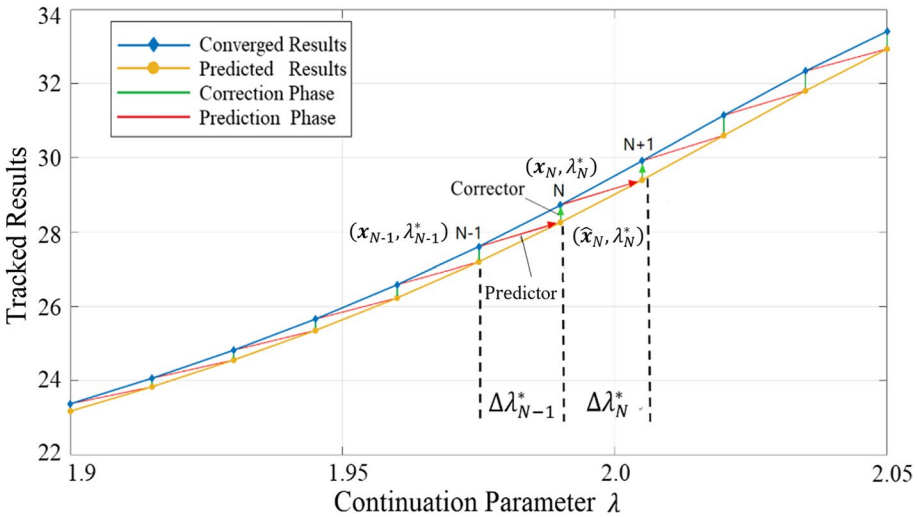

Fig. 5 Path tracking based on the continuation method

$$\boldsymbol{J}\boldsymbol{t} = 0, \tag{9}$$

$$\boldsymbol{t}\boldsymbol{t}^T = 1, \tag{10}$$

where $\boldsymbol{J} = [\boldsymbol{J}_{\boldsymbol{x}}, \boldsymbol{J}_{\lambda^*}] = [\frac{\partial \boldsymbol{H}}{\partial(\boldsymbol{x})}, \frac{\partial \boldsymbol{H}}{\partial(\lambda^*)}]$ is the Jacobian matrix. Equations (9) and (10) can be solved to yield:

$$\begin{cases} \boldsymbol{t}_{\boldsymbol{x}} = \pm \frac{1}{\sqrt{1+\|\boldsymbol{v}\|^2}} \\ \boldsymbol{t}_{\lambda^*} = \boldsymbol{t}_{\boldsymbol{x}} \boldsymbol{v} \end{cases}, \tag{11}$$

where $\boldsymbol{v} = -\frac{\partial \boldsymbol{H}}{\partial(\boldsymbol{x})} / \frac{\partial \boldsymbol{H}}{\partial(\lambda^*)}$. The predicted solution $(\widehat{\boldsymbol{x}}_N, \lambda_N^*)$ at the N^{th} step can be calculated using the tangent vector $\boldsymbol{t}$ as follows:

$$\begin{cases} \widehat{\boldsymbol{x}}_N = \boldsymbol{x}_{N-1} + \Delta\lambda^* \boldsymbol{t}_{\boldsymbol{x}} \\ \lambda_N^* = \lambda_{N-1}^* + \Delta\lambda^* \boldsymbol{t}_{\lambda^*} \end{cases}, \tag{12}$$

where $\Delta\lambda^*$ is the step size chosen for each iteration. Equation (11) implies that two tangent vectors, pointing in opposite directions, can exist along the tracking curve. This poses a question on the selection of the correct direction for the tangent vector $\boldsymbol{t}$ for the implementation of the CM method, and this is usually decided by the physics of the engineering application to which the method is applied. In the present aeroelastic analysis, the continuation parameter is often chosen to be the airspeed for mode tracking tasks. For this case then the direction of the tangent vector in Eq. (11) can be selected as the one for which the airspeed has a higher value. Once the predicted solution is obtained, the standard Newton–Raphson method for nonlinear equations is used as the corrector algorithm as follows:

$$\left\{\widehat{\boldsymbol{x}}_N^{i+1}\right\} = \left\{\widehat{\boldsymbol{x}}_N^{i}\right\} - \left\{\left[\frac{\partial \boldsymbol{H}}{\partial(\boldsymbol{x})}\right]_N^{-1}\right\}^i \boldsymbol{H}\left(\widehat{\boldsymbol{x}}_N^i, \lambda^* = \lambda_N^*\right), \tag{13}$$

because of its proven efficiency for solving nonlinear equations, provided a reasonable initial guess can be given from the predictor. Figure 6 shows the corrector phase based on the Newton–Raphson method in which the iterations from Eq. (13) are repeated until the convergence criteria, i.e., $\left|\widehat{\boldsymbol{x}}_N^{i+1} - \widehat{\boldsymbol{x}}_N^{i}\right| < 10^{-5}$, is satisfied or the maximum number of iterations is reached. An obvious advantage of CM is that it appears to be less sensitive to the initial values provided compared to the Newton–Raphson method and hence can be globally convergent under certain conditions mentioned in Trajkovic et al. [18]. This is extremely important for solving engineering problems for which the initial guess is often difficult to set. The main drawback of the CM is that it can be computationally intensive since the predictor and corrector phases require enormous computation time for the iterations.

3.4 Step size control algorithm

When the continuation method is applied for tracking all the aeroelastic modes in the frequency domain to estimate the flutter boundary, the step size $\Delta\lambda_N^*$ of the continuation parameter which is chosen as the incremental airspeed is crucial for achieving a balance

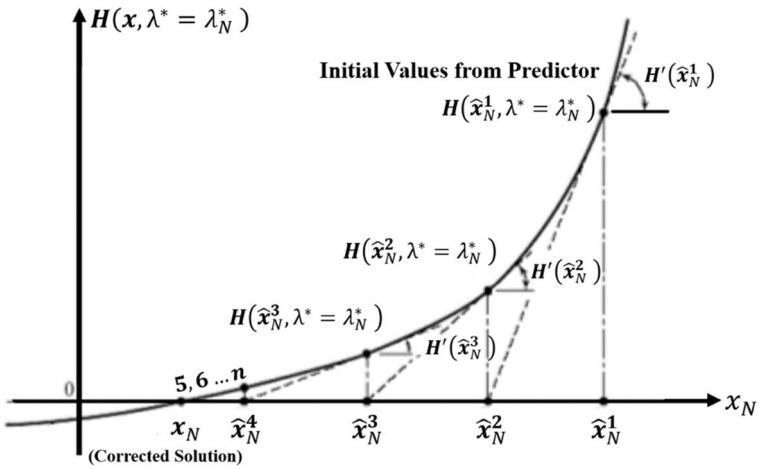

Fig. 6 Corrector phase based on the Newton–Raphson method in the continuation method

between efficiency, accuracy, and stability of the computation. An improper large step size could lead to divergence while too small a step size may sacrifice efficiency substantially. In the mode tracking process, the potential divergence in the numerical scheme could occur when a large step size is chosen near the region where multiple aeroelastic modes cluster or when the aeroelastic modes get switched with one another, which is known as mode switching. For this reason, the step size in the present study is adjusted based on a step size control algorithm developed and applied in Yu et al. [16, 17], which enables the step size to change adaptively for typical situations often encountered in the aeroelastic analysis. The basic principles are summarized as follows. Consider σ_i^N and σ_j^N to be the corrected solutions at the N^{th} step of two tracking curves labeled with indices i and j, respectively. Compared to the classical mode tracking algorithm where the structural modes are tracked successively, in the present study, the structural modes are tracked simultaneously so that the closeness index Ω_σ defined as

$$\Omega_\sigma = \left| \frac{\sigma_i - \sigma_j}{1 + \sigma_i \sigma_j} \right|, \tag{14}$$

could be computed at each step using σ_i^N and σ_j^N. On the basis of the estimated value of the closeness index, Ω_σ, the step size $\Delta\lambda_N^*$ is then adjusted according to the satisfaction of the following condition:

$$\Delta\lambda_N^* = \begin{cases} \eta\Delta\lambda_0^*, & 0 < \Omega_\sigma \leq \epsilon \\ \Delta\lambda_0^*, & \Omega_\sigma > \epsilon \end{cases}, \tag{15}$$

where ϵ is the closeness radius for which the recommended value is in the range 0–0.2, η is a small constant, normally chosen as 0 to 0.2, and $\Delta\lambda_0^*$ is the initial step size of the continuation parameter. Once two different modes become too close to one another, i.e., $|\Omega_\sigma| \leq \epsilon$, the step size is adjusted automatically to a smaller value, i.e., $\eta\Delta\lambda_0^*$ to avoid the divergence or misidentification of modes caused by the mode switching phenomenon. The parameter ϵ determines the specific location and condition to initiate the adaptive step size control algorithm to reduce the step size, thus avoiding the potential divergence of the CM algorithm during simultaneous tracking of multiple modes. Parameter η, on

the other hand, determines the ratio of the reduced step size to the original step size $\Delta\lambda_0^*$. In general, as the parameter ϵ decreases and the parameter η increases, the number of iterations required by the CM solver is reduced, which results in higher computational efficiency, albeit at the expense of algorithmic stability to some extent. Therefore, in practical mode tracking tasks, a suitable combination of parameters ϵ and η must be selected according to specific circumstances to achieve the best balance between computational efficiency and algorithm stability. As an example, the mode tracking analysis is conducted on a test case introduced in Yu et al. [17] based on the continuation method using both fixed step size and adaptive step size. The corresponding results are shown in Fig. 7 (a) (fixed step size) and Fig. 7 (b) (adaptive step size), respectively. As can be observed in Fig. 7 (a), the misidentification of modes occurs in the numerical scheme. The reason for this failure is that by using a fixed and too large step size, the continuation algorithm fails to identify two switched modes, i.e., Mode 1 and Mode 2, when the airspeed reaches around 19 m/s. However, the same phenomenon is handled properly and both modes are identified correctly in Fig. 7 (b) since the step size $\Delta\lambda^*$ is adaptively reduced from 0.25 m/s to 0.05 m/s when it approaches close to the switching regions as shown in the red box.

The flutter speed V_f and the corresponding flutter frequency ω_f are usually of main interest in most of the mode tracking analysis. In order to get better accuracy of estimation in which the V_f and ω_f are interpolated from the neighborhood points near the flutter region, a smaller step size is preferred and chosen according to Eq. (16).

$$\Delta\lambda_N^* = \begin{cases} \eta\Delta\lambda_0^*, & -\epsilon \leq \sigma_i \leq \epsilon \\ \Delta\lambda_0^*, & \sigma_i > \epsilon, \sigma_i < -\epsilon \end{cases}. \tag{16}$$

3.5 Application of continuation method in flutter analysis

The proposed CM is applied to the governing equations defined in Eq. (7). For each fixed Mach number, the $\boldsymbol{A}.\boldsymbol{I}.\boldsymbol{C}(M_a, k)$ matrices are computed using the aerodynamic solver for reduced frequencies k in the range $0 \leq k \leq 1.5$. Since the original $\boldsymbol{A}.\boldsymbol{I}.\boldsymbol{C}(M_a, k)$ matrices can only be computed for a series of discrete reduced frequencies corresponding to a fixed Mach number M_a, the Rational Function Approximation (RFA) method outlined

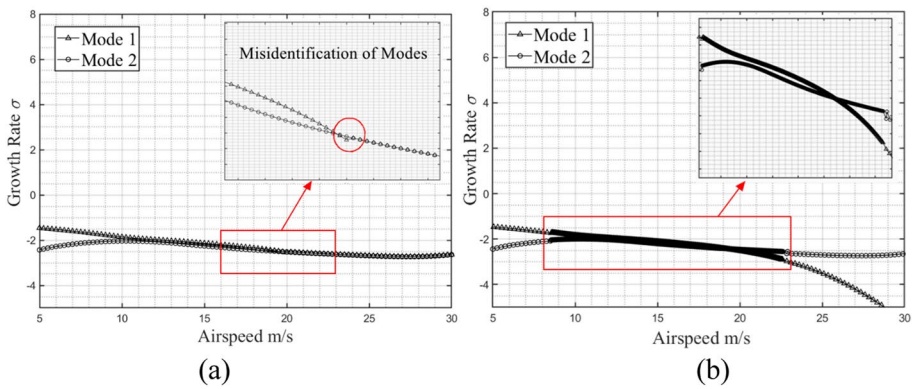

Fig. 7 Mode tracking using the continuation method (**a**) fixed step size - failure (**b**) adaptive step size - success

in the *ZAERO Manual* [26] is used to transform the $\boldsymbol{A.I.C}(M_a, k)$ matrices from the frequency domain to the Laplace domain using the classical Roger's formula as follows:

$$[\boldsymbol{A.I.C}(p)] = [\boldsymbol{A}_0] + [\boldsymbol{A}_1]p + [\boldsymbol{A}_2]p^2 + \sum_{l=3}^{n_l+2} [\boldsymbol{A_l}]\frac{p}{p+\Upsilon_{l-2}}, \tag{17}$$

where $p = sb/V$ is the scaled Laplace variable, n_l is the number of lag terms, and γ_i is the root value of each lag term which is chosen using the empirical formula shown in Ref. [26], i.e.,

$$\gamma_i = 1.7k_{max}\left(\frac{i}{n_l+1}\right)^2. \tag{18}$$

For the present study, $n_l = 3$. When the $\boldsymbol{A.I.C}(M_a, k)$ matrices are transformed from the frequency domain to the Laplace domain, formulations based on any of the approaches based on the Least Squares (LS) method, Modified Matrix Pade (MMS) or the Minimum State (MS) can be used for curve fitting as shown in Tiffany and Adams [27]. The reduced-order system equations are then transformed to:

$$\overline{\boldsymbol{M}}\ddot{\boldsymbol{q}} + \overline{\boldsymbol{D}}\dot{\boldsymbol{q}} + \overline{\boldsymbol{K}}\boldsymbol{q} - q_{dyn}(\boldsymbol{A}_3\boldsymbol{Y}_1 + \boldsymbol{A}_4\boldsymbol{Y}_2 + \boldsymbol{A}_5\boldsymbol{Y}_3) = 0, \tag{19}$$

where $\boldsymbol{Y_i} = \frac{p}{p+\Upsilon_i}\boldsymbol{q}$, $\overline{\boldsymbol{M}} = \boldsymbol{M} - q_{dyn}\boldsymbol{A}_2\left(\frac{b}{V}\right)^2$, $\overline{\boldsymbol{D}} = -q_{dyn}\boldsymbol{A}_1\left(\frac{b}{V}\right)$ and $\overline{\boldsymbol{K}} = \boldsymbol{K} - q_{dyn}\boldsymbol{A}_0$. The state-space form of the governing equations can be written as:

$$\dot{\boldsymbol{X}} = \boldsymbol{A}\boldsymbol{X}, \tag{20}$$

where $\boldsymbol{X} = \left[\boldsymbol{q}\dot{\boldsymbol{q}}\dot{Y}_1\dot{Y}_2\dot{Y}_3\right]$ and the matrix $\boldsymbol{A}$ is

$$\boldsymbol{A} = \begin{pmatrix} \boldsymbol{0} & \boldsymbol{I} & \boldsymbol{0} & \boldsymbol{0} & \boldsymbol{0} \\ -(\overline{\boldsymbol{M}})^{-1}\overline{\boldsymbol{K}} & -(\overline{\boldsymbol{M}})^{-1}\overline{\boldsymbol{D}} & q_{dyn}(\overline{\boldsymbol{M}})^{-1}\boldsymbol{A}_3 & q_{dyn}(\overline{\boldsymbol{M}})^{-1}\boldsymbol{A}_4 & q_{dyn}(\overline{\boldsymbol{M}})^{-1}\boldsymbol{A}_5 \\ \boldsymbol{0} & \boldsymbol{I} & -(V\gamma_1\boldsymbol{I})/b & \boldsymbol{0} & \boldsymbol{0} \\ \boldsymbol{0} & \boldsymbol{I} & \boldsymbol{0} & -(V\gamma_2\boldsymbol{I})/b & \boldsymbol{0} \\ \boldsymbol{0} & \boldsymbol{I} & \boldsymbol{0} & \boldsymbol{0} & -(V\gamma_3\boldsymbol{I})/b \end{pmatrix},$$

where $\boldsymbol{I}$ is the identity matrix. The main drawback of the RFA method is the trade-off between the finite number of aerodynamic lags n_l and the accuracy of the approximation. For the flutter analysis of the complex wing configurations using the CM, the approximation errors for $\boldsymbol{A.I.C}(M_a, k)$ using the RFA Method could become large to have an impact on the accuracy of final solutions. For this purpose, an alternative approach is to calculate $\boldsymbol{A.I.C}(M_a, k)$ in the discrete reduced frequency domain by coupling the aerodynamic solver directly and updating the governing equations simultaneously for each iteration of the mode tracking process. Figure 8 shows the flow chart of combining the CM solver with both the structural and aerodynamic solvers for mode tracking in facilitating the flutter analysis reported in this study.

4 Results and discussions

In this section, the salient features of the CM with adaptive step are demonstrated. The first four natural mode shapes without applied loads and the corresponding natural frequencies are computed for the JSM wing-pylon-nacelle with engine mass model referred to as

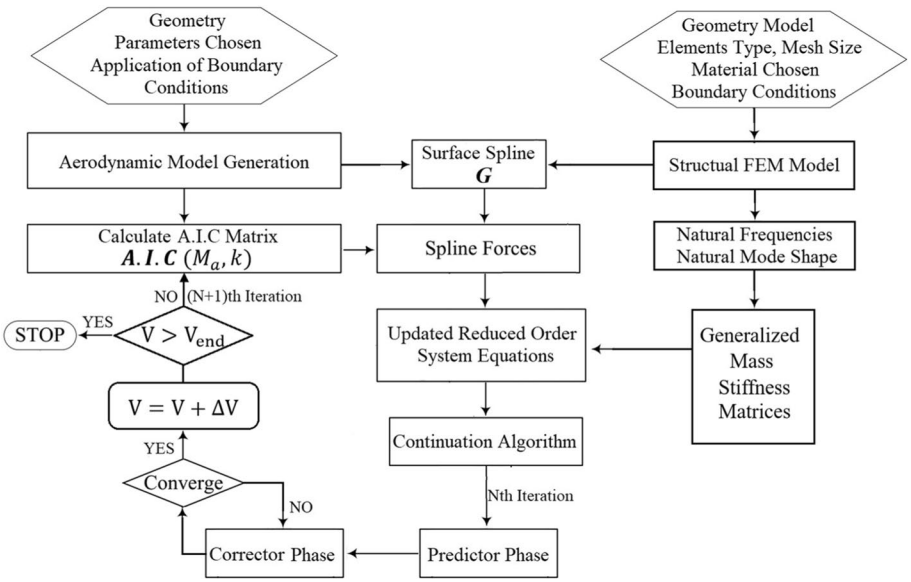

Fig. 8 Flow chart of applying the continuation method in mode tracking for flutter analysis

the JAXA model and the clean wing (without pylon-nacelle and engine). The differences in the mode shapes are compared for both configurations to assess the differences that result when an engine-pylon effect is included in the clean wing. Mode tracking using the continuation method with adaptive step is compared with that using the approaches based on eigenvalue analysis and the *p-k* method in *NX Nastran* for the flutter analysis of these configurations. The mode switching phenomenon is also demonstrated for selected flight conditions to illustrate how improper handling of this phenomenon can lead to numerical difficulties in flutter analysis to show the advantage of the Continuation Method with adaptive step.

4.1 Fundamental modes and natural frequencies

The first four natural frequencies and the first two nacelle modes of the JSM_*enp* model and those of the JSM_*c* model are computed as listed in Table 1, and the corresponding mode shapes are shown in Fig. 9 and Fig. 10, respectively. As shown in Table 1, the natural frequencies of the first three fundamental modes, i.e., the 1st bending, 1st torsion, and 2nd bending modes, have increased compared to those of the clean wing model, while the natural frequency of the 4th fundamental mode, which is the 3rd bending mode, decreased to 15.356 Hz from 16.335 Hz, corresponding to the clean wing. Generally, adding an external mass could lower the modal frequencies of the original structure. However, this is not consistent with our case due to the presence of the engine nacelle and the corresponding structural reinforcements for the engine installation. They affect the wing structural mass distribution and stiffness properties in a way that takes an opposite effect on the first three modal frequencies.

Table 1 Natural frequencies of the clean wing and wing with engine nacelle

#	Mode Frequencies (Nastran)	With Engine Nacelle JSM_*enp* Model (Hz)	Clean Wing JSM_*c* Model (Hz)
1	1st bending	1.366	1.1381
2	2nd bending	6.732	6.437
3	1st torsion	12.603	10.768
4	3rd bending	15.356	16.335
5	Nacelle pitching	2.528	-
6	Nacelle rolling	4.446	-

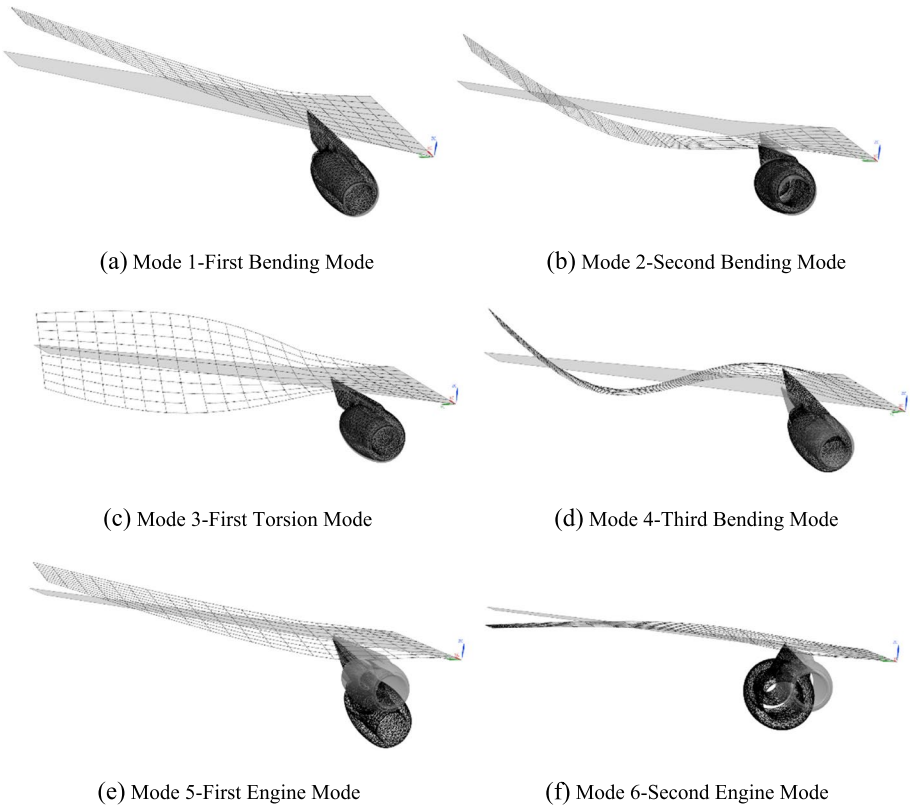

(a) Mode 1-First Bending Mode (b) Mode 2-Second Bending Mode

(c) Mode 3-First Torsion Mode (d) Mode 4-Third Bending Mode

(e) Mode 5-First Engine Mode (f) Mode 6-Second Engine Mode

Fig. 9 The first six natural mode shapes of the JSM_*enp* model

4.2 Mode tracking results in flutter analysis

The flutter speed V_f is estimated by calculating the complex eigenvalues of the matrix $\boldsymbol{A}$ of Eq. (20) for a range of flight speeds V. The occurrence of instability can be inferred if the real part of the eigenvalues changes from a negative to a positive value while the imaginary part of the eigenvalues provides an estimate of the frequency of the oscillation as a result of the instability. It should be noted that the static divergence may also occur if the imaginary part is zero when the real part of the eigenvalue becomes positive. Figures 11 and 12 show the variation of the real part of the eigenvalues vs. airspeed from the mode tracking results based on the eigenvalue analysis approach, i.e., the *p-k* method for the JSM_*c* and JSM_*enp* models, respectively, for a low-speed flight at a Mach number of 0.1. In Fig. 11, mode 1 corresponds to the flutter mode since it reaches flutter (as the

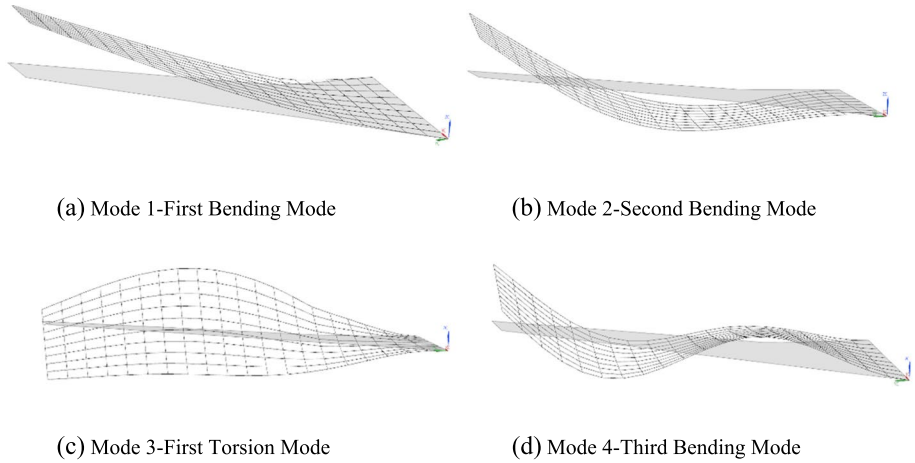

Fig. 10 The first four natural mode shapes of the JSM_*c* model

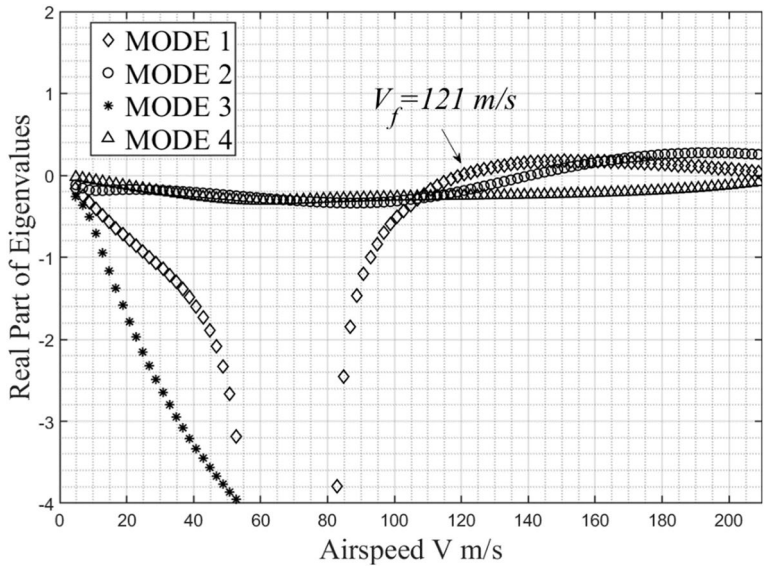

Fig. 11 Mode tracking for JSM_*c* model at Mach number 0.1

real part of the eigenvalue goes to zero) at 121 m/s before mode 2 which remains stable until about 141 m/s for a flight Mach of 0.1. However, from Fig. 12 corresponding to the JSM_*enp* model for which the mass and stiffness matrices are different from those of the JSM_*c* model, it can be seen that mode 2 becomes the flutter mode since it reaches the flutter speed at 93 m/s earlier than mode 1 which reaches flutter at about 123 m/s. The inclusion of the engine nacelle appears to reduce the flutter speed by around 23%.

Usually, when the tracked aeroelastic mode is labeled as "mode *n*", e.g., "mode 1" in Fig. 11, it doesn't refer to the pure structural mode when $V \neq 0$ m/s, instead it indicates this aeroelastic mode under this condition arises continuously from the 1st structural mode shape. It should be noted that when the flutter occurs, the corresponding flutter mode is in fact a combination of all the structural modes with different contributions. For example, Fig. 13 presents the mode shape of JSM_*c* model when flutter occurs,

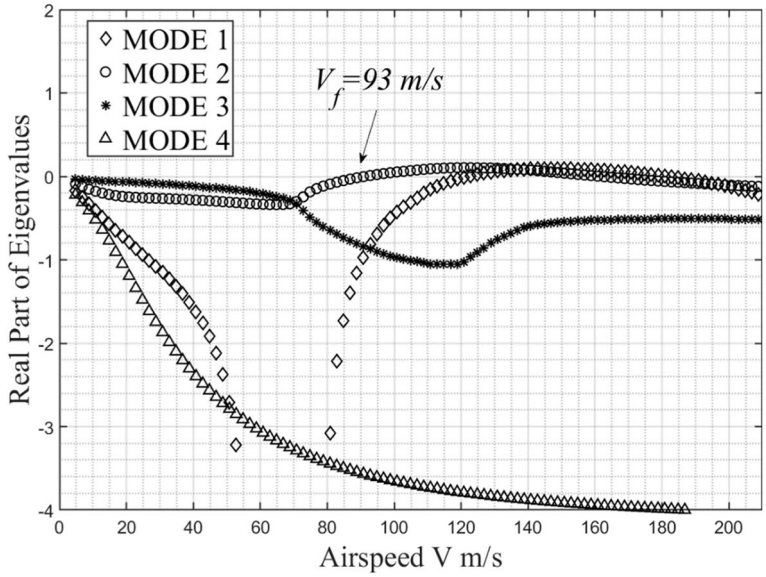

Fig. 12 Mode tracking for JSM_*enp* model at Mach number 0.1

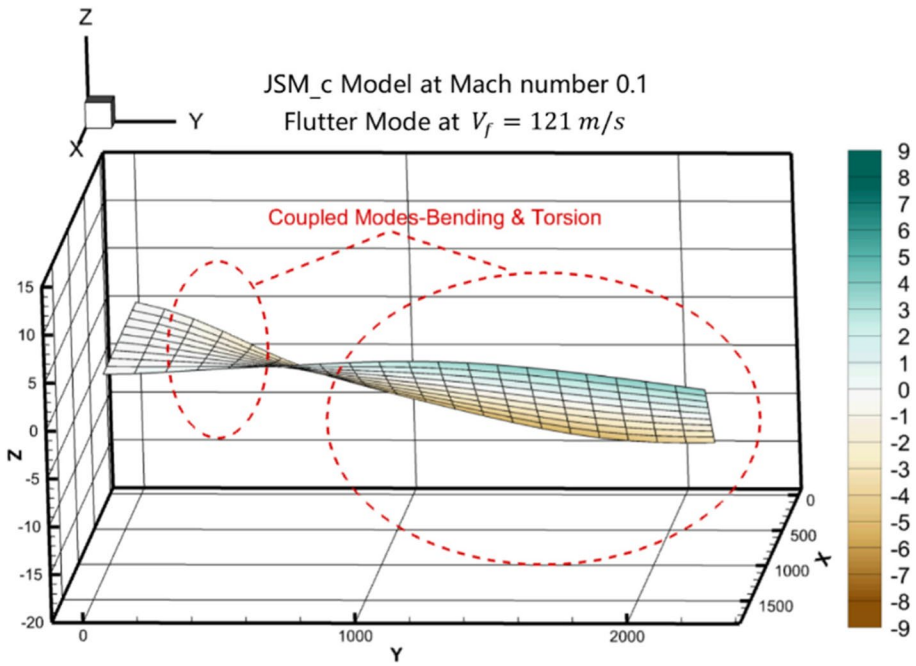

Fig. 13 Flutter mode shape of JSM_*c* model at Mach number 0.1

i.e., flutter mode at $M_a = 0.1$. From the mode tracking results shown in Fig. 11, it is the mode 1, i.e., the 1st bending mode, that goes to flutter at $V_f = 121$ m/s. However, as can be seen in Fig. 13, the flutter mode is actually a bending-torsion type since it receives contributions from both bending and torsion modes.

The first four natural modes are tracked with the adaptive step size in the continuation method continuously to estimate the flutter boundary corresponding to different

free-stream Mach numbers. The solutions for the reduced order governing equation Eq. (7b) using the continuation method can be expressed as follows:

$$\boldsymbol{\eta} = \overline{\boldsymbol{\eta}} e^{\lambda t}, \tag{21}$$

where $\overline{\boldsymbol{\eta}}$ is the complex eigenvector representing the aeroelastic modes corresponding to different airspeeds V and $\lambda = \sigma + i\omega$, in which σ is the growth rate of oscillation which indicates the instability when $\sigma > 0$, and ω is the corresponding angular frequency of oscillation. Substituting Eq. (21) into the governing Eq. (7b) results in a nonlinear continuation equation to be solved, i.e.,

$$H = \left[\lambda^2 \boldsymbol{M_r} + \boldsymbol{K_r} - q_{dyn} \boldsymbol{A.I.C_r}(M_\mathrm{a}, k)\right] \overline{\boldsymbol{\eta}} = 0. \tag{22}$$

A continuous tracking curve between the airspeed V and growth rate σ as well as the oscillation frequencies ω can be obtained by solving Eq. (22) iteratively. Figures 14 and 15 respectively show the variation of the growth rate σ for a range of airspeeds corresponding to each mode from the mode tracking results based on this continuation method with adaptive step for both the JSM_*c* and JSM_*enp* models at a Mach number of 0.5.

From Figs. 14 and 15, the flutter speed V_f estimated from the continuation method using two adaptive step sizes, i.e., $\Delta\lambda^*_{max} = 2$ m/s, $\Delta\lambda^*_{min} = 0.5$ m/s, for the JSM_*c* and JSM_*enp* models are 116.4 m/s and 88.7 m/s, respectively. Table 2 compares the flutter speed estimated using four approaches, i.e., the eigenvalue analysis using RFA approximation, the *p-k* method within the Aeroelasticity Module in *Nastran*, the CM solver with adaptive step size and the CM solver with a small fixed step size. The main reason for the minor differences in the flutter speed estimates stems from the number of interpolation points clustered around the flutter point where $\sigma = 0$ and the errors caused by the RFA approximation. The estimates from the continuation method appear to be the most robust result since the step size can either be fixed to a small value or adaptively reduced around the flutter point to increase the accuracy. In addition, compared to the

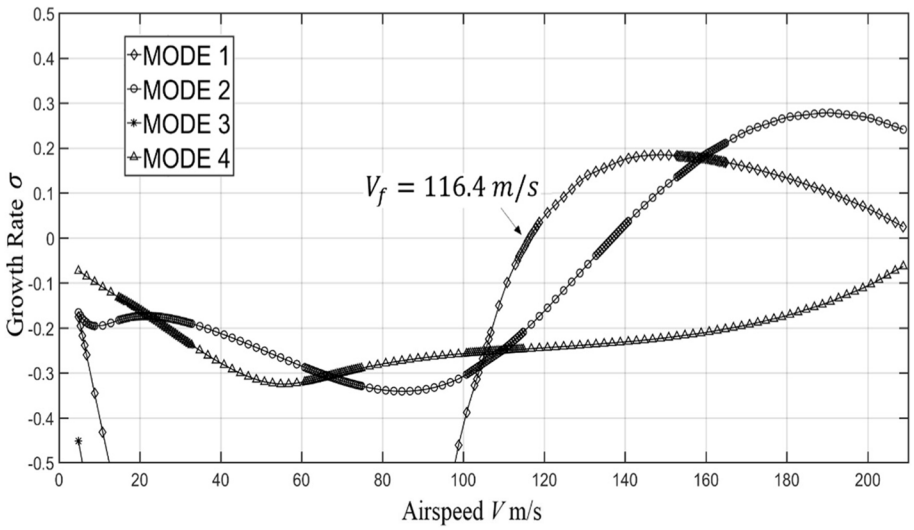

Fig. 14 Mode tracking for JSM_*c* model using the continuation method at Mach number 0.5

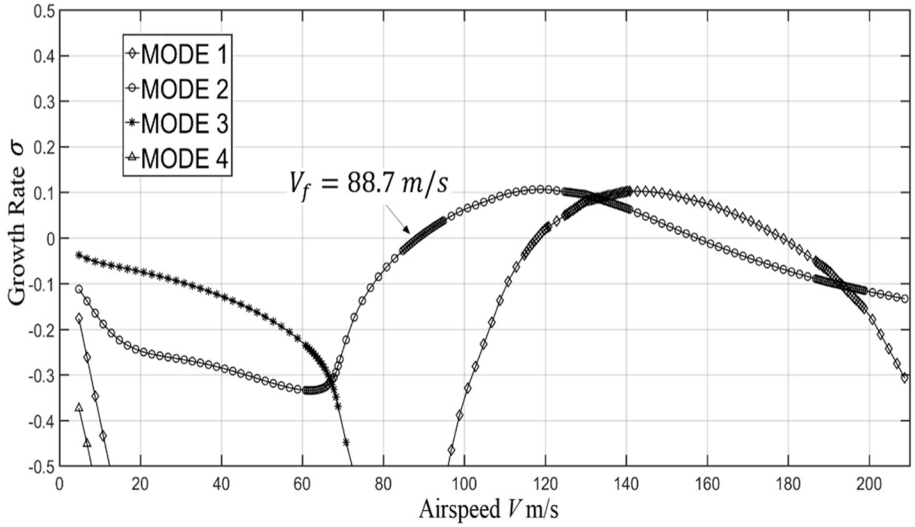

Fig. 15 Mode tracking for JSM_*enp* model using the continuation method at Mach number 0.5

Table 2 Estimates of flutter speeds of the JSM_*c* and JSM_*enp* models

#Case	Eigenvalue Analysis	*p-k* Method Nastran based on DLM	CM with adaptive step size $\Delta\lambda^* = 2$ and 0.5	CM with fixed step size $\Delta\lambda^* = 0.5$
Clean Wing (m/s)	119	115	116.4	116.4
Wing with Engine (m/s)	91	90	88.7	88.7
Number of Steps	-	-	229	551
Computation Time (Intel Core i7-10700 @ 3.80 GHz)		13.2 s	34.3 s	83.6 s

estimates from CM using a small fixed step size, i.e., $\Delta\lambda^* = 0.5$, using adaptive step sizes of $\Delta\lambda^* = 2$ and 0.5 results in the same flutter speed while significantly reducing the number of steps required by more than 50%. This obvious reduction in the number of steps required in CM boosts the computational efficiency of the method substantially and hence will benefit the preliminary design work where the mode tracking task with different system parameters must be done repeatedly.

The continuation method also enables the tracking of the variation of the frequency components of each mode for a range of airspeed and these are shown in Figs. 16 and 17 for the JSM_*c* and JSM_*enp* models respectively at a Mach number of 0.5. As the flight speed approaches the flutter point $V_f = 119.8$ m/s, it can be seen that the oscillation frequencies of mode 3 and mode 4 intersect with one another at around 16 Hz for the JSM_*c* model, and for the JSM_*enp* model the frequency coalescence occurs between mode 2 and mode 3 at around 6 Hz, which appears to be lower than that of the JSM_*c* model by 62.5%.

Figure 18 shows the computed flutter speed of the JSM_*c* and JSM_*enp* models with flight Mach numbers using the CM with an adaptive step method. It appears that if the wing is fitted with an engine nacelle and pylon, the flutter speed decreases substantially

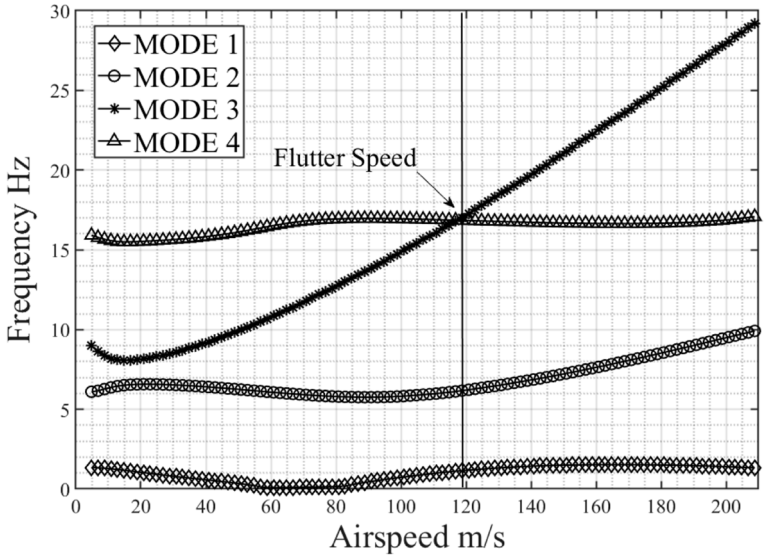

Fig. 16 Frequency tracking for JSM_*c* model at Mach number 0.5

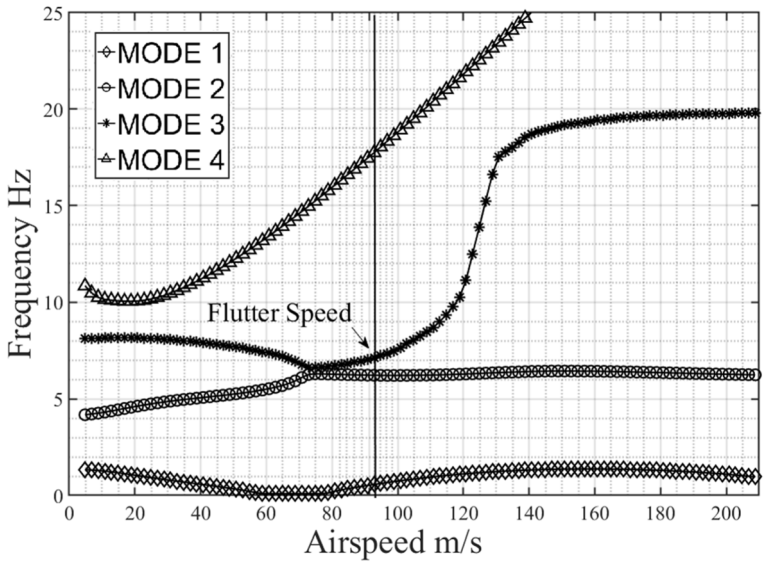

Fig. 17 Frequency tracking for JSM_*enp* model at Mach number 0.5

by about 25%–30% in the subsonic flight regime and about 5% in the low-end supersonic flight regime.

4.3 Mode switching phenomenon

The mode switching phenomenon is generally observed in the mode tracking task. It happens when the variation of the growth rate of several different aeroelastic modes with flight speed gets closer to one another, resulting in the intersection of these curves corresponding to different modes at certain points in the growth rate vs. airspeed space. It is a crucial task to correctly recognize the aeroelastic mode tracking curves from each intersection point to understand the development of flutter for each aeroelastic mode.

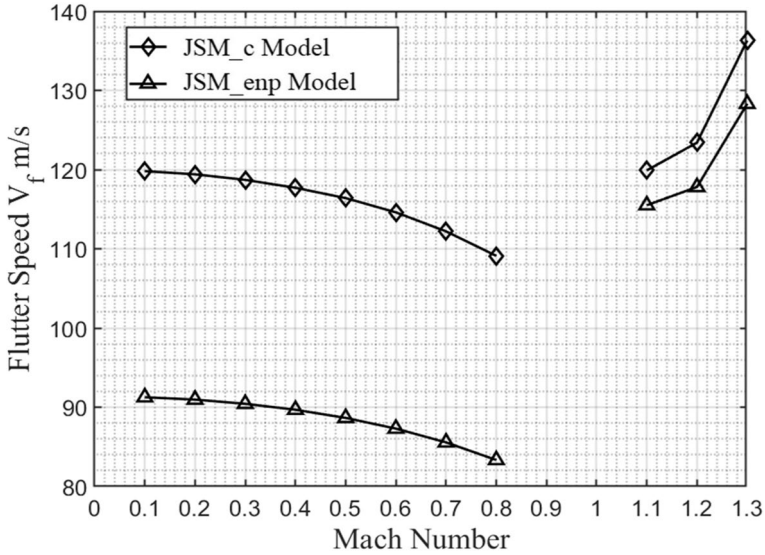

Fig. 18 Flutter speed of JSM_*c* and JSM_*enp* models with Mach number

However, traditional methods such as the eigenvalue analysis or *p-k* method may sometimes cause difficulties because, for most situations of this type, a natural solution will be to connect those points of the solution which belong to one aeroelastic mode manually to avoid the possibility of misidentification. Such a manual approach tends to be cumbersome and in some cases, it may even be difficult to differentiate the curves corresponding to different modes apart correctly when they all start to switch near a particular point. This is shown in Fig. 19, which shows the results of the mode tracking for the growth rate σ of four aeroelastic modes vs. airspeed V using the *p-k* method for the JSM_*c* at a flight Mach number M_a of 1.1. It can be seen here that when the airspeed V varies from 0 to 100 m/s, the mode tracking curves corresponding to modes 2 and 4 get very close to one another and switch twice at the airspeed of 25 m/s and 65 m/s. When the airspeed reaches around 105 m/s, the curves corresponding to modes 1, 2, and 4 switch at the point indicated by the red circle in Fig. 19. However, this difficulty proves to be well handled in Fig. 20, which shows the mode tracking results of the same case in Fig. 19 by using the continuation method with adaptive step size. In other situations, the misidentification of aeroelastic mode tracking curves can even lead to potential numerical errors in flutter analysis. Though the *Nastran* Aeroelasticity Module (SOL 145) has a built-in algorithm to assist in differentiating the mode tracking curves and connecting them automatically, it is not robust enough, especially when there are too many selected modes to be tracked. As an example, Fig. 21 shows the mode tracking results of the JSM_*c* model at a Mach number 1.2 computed using the built-in *p-k* method in the aeroelastic solver in *Nastran*. As can be seen, this algorithm, which is used to connect the mode tracking curves, fails to differentiate apart mode 2 and mode 5, and also mode 3 and mode 4 after the mode switching event occurs at the flight speed V of 100 m/s. This eventually leads to discontinuities and misidentification along the tracking curves, which can be seen in Fig. 21. In the present study, this issue is easily and well managed by using the continuation method as shown in Fig. 22, which appears to be very robust

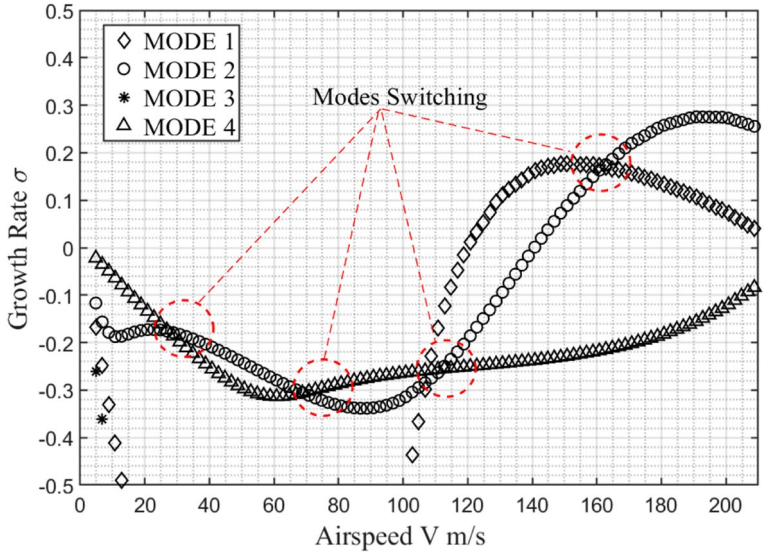

Fig. 19 Mode tracking for JSM_*c* model using the *p-k* method at Mach number 1.1

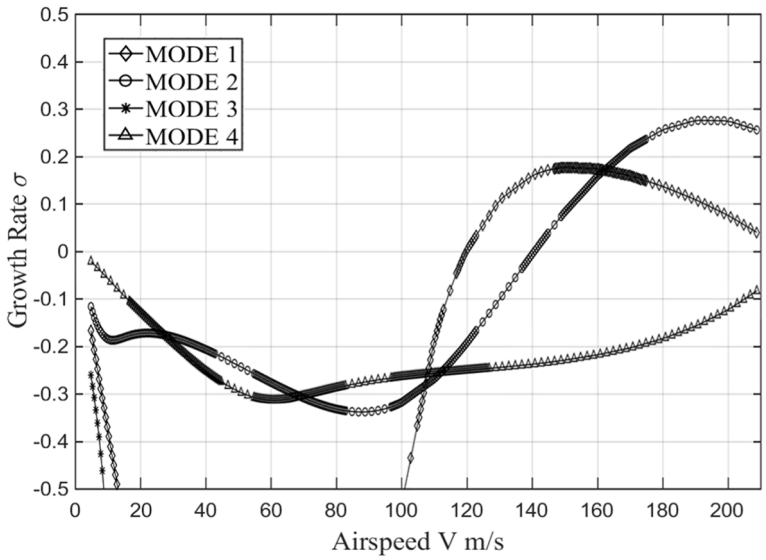

Fig. 20 Mode tracking for JSM_*c* model using the CM with adaptive step at Mach number 1.1

in recognizing the mode switching phenomenon. This is because the predictor solver of the continuation method can predict the right direction of each tracking curve based on the previous solution points, and hence can automatically connect these points one by one.

5 Conclusions

This study employs the utilization of the continuation method and an adaptive step size control algorithm to perform aeroelastic analysis on a wing-pylon-nacelle configuration in subsonic and low supersonic flight regimes. The aerodynamic forces are estimated with different reduced frequencies using linearized unsteady small-disturbance potential flow

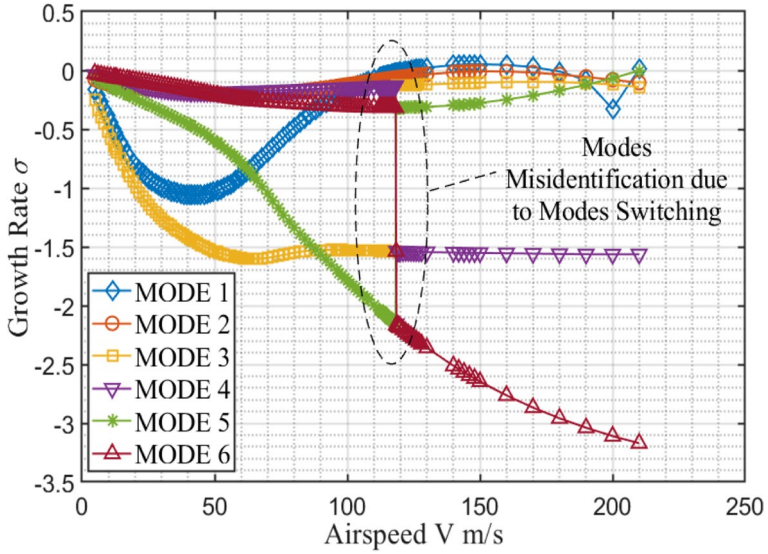

Fig. 21 Mode tracking for JSM_*c* model using the *p-k* method at Mach number 1.2

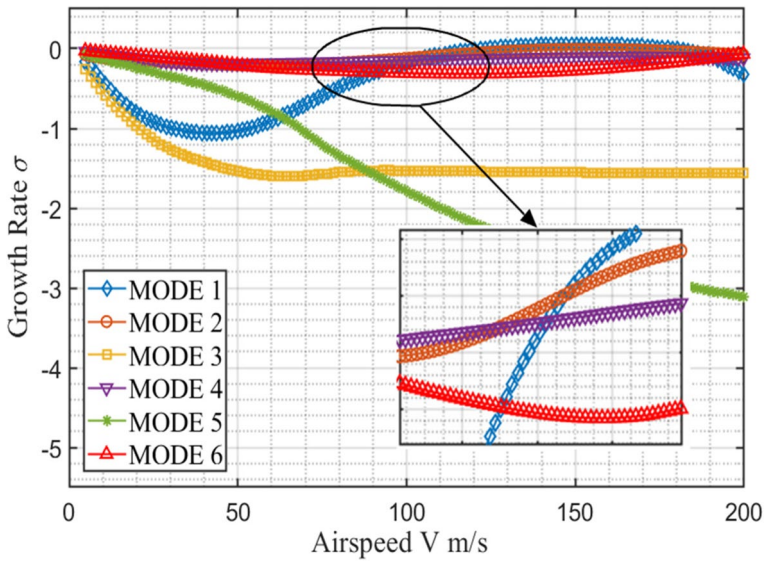

Fig. 22 Mode tracking for JSM_*c* model using the continuation method at Mach number 1.2

models. The state space form of the system equations based on the RFA method combined with the continuation method is employed for the analysis of flutter. To illustrate its efficiency in mode tracking and mode switching, the results obtained from the continuation method are compared with those obtained from the conventional *p-k* method. Firstly, it has been demonstrated that the continuation method with adaptive step size achieves better accuracy in estimating the flutter speed compared to traditional eigenvalue analysis and the *p-k* method. This is due to the increased number of interpolation points near the flutter occurrence region resulting from step size reduction. Moreover, the continuation method exhibits a distinct advantage in identifying the "mode switching" phenomenon, which can lead to aeroelastic mode development misidentification that is often encountered with

the *p-k* method and the eigenvalue method. Incorporating the adaptive step size based on automatic detection of the mode switching phenomenon in the implementation of the continuation method significantly facilitates distinguishing between various instances of mode switching. It should also be noted that compared to traditional methods, the proposed algorithm in this paper will consume more computation resources as stated in Table 2, but the benefits brought are equally significant. These advantages are especially true when accounting for the following two factors in practice: (1) in the preliminary design work where the mode tracking task with different system parameters must be done repeatedly, any algorithmic failure caused by the misidentification of modes can consume an extra abundance of time and even manual correction by researchers; (2) with the continual augmentation of computer processing power and the utilization of parallel computing using multiple CPUs, the disparity in computational efficiency between the classical methods and the proposed algorithm will further decline.

Another point that the author has to emphasize here is that the proposed method in this article, namely the adaptive step size CM algorithm, operates successfully in the frequency domain regardless of the different aerodynamic models used in different flow regions. This is because whether the linearized aerodynamic responses is through the DLM method (applicable to subsonic regions), ZONA51 method (applicable to supersonic regions), or the harmonic motion method/filtered impulse function method based on CFD simulations (applicable to transonic regions), the format of the reduced order governing equations for the JSM wing, i.e., Eq. (7b), remains unchanged. To put it more simply, in the frequency domain, the form of the linearized aerodynamic influence coefficient matrices, i.e., $\boldsymbol{A.I.C}(M_a, k)$, in all flow regions remains unchanged.

Furthermore, a significant decrease in flutter speed is observed in both the subsonic and lower supersonic regimes following the application of an engine nacelle to the JSM wing model. This phenomenon can largely be attributed to the substantial mass distribution changes that result from the addition of the nacelle, leading to a negative impact on the dynamic stabilities of the wing structure. Consequently, this study serves as a motivation for future use of the continuation method with adaptive time step to evaluate nonlinear flutter characteristics under transonic flow flight and high-fidelity aerodynamic modeling based on the full Navier–Stokes equations.

6 Nomenclature

$\boldsymbol{G}$ Spline matrix
$\boldsymbol{H}$ Continuation method equations
$\boldsymbol{J}$ Jacobian matrix
$\boldsymbol{K}$ Stiffness matrix
$\boldsymbol{M}$ Mass matrix
$\boldsymbol{M_r}$ Reduced order/generalized mass matrix
$\boldsymbol{K_r}$ Reduced order/generalized stiffness matrix
$\boldsymbol{\eta}$ Modal coordinates
$\boldsymbol{q}$ Displacement vector
$\boldsymbol{t}$ Tangent vector in the predictor of continuation algorithm
$\boldsymbol{\Phi}$ Modal matrix
k Reduced frequency

M_a Mach number
n_l Number of lag terms
p Scaled Laplace variable
q_{dyn} Dynamic pressure
V Airspeed
V_f Flutter velocity
φ Disturbance velocity potential function
λ Eigenvalue
λ^* Continuation parameter
ρ Air density
Ω_σ Closeness index between the growth rate in mode tracking
γ_i Root value of each lag term
ϵ Closeness radius
η Small constant to determine the step size in continuation method solver
$\Delta\lambda_N^*$ Step size of continuation parameter in N^{th} iteration
ω Oscillating frequency
ω_f Flutter frequency

Acknowledgements
Not applicable.

Authors' contributions
QY contributed to the analysis, mathematical modelling, simulations and manuscript preparation. MD conceived the application problem assessing the adaptive CM method, advised on the computed data analysis with constructive discussions, and assisted in the writing of the manuscript. BCK contributed to the conception of the study and helped write and improve the manuscript significantly.

Funding
The research results presented in this paper is funded by the Innovation Fund of the Engineering Research Center of Integration and Application of Digital Learning Technology, Ministry of Education (1221043), the Youth Research Project - The Open University of China (Q21A0009) and the Adult continuing education research program - China Adult Education Association (2021-326Y).

Availability of data and materials
Some data, models, or codes generated or used during this study are available from the corresponding author by request.

Declarations

Competing interests
The authors declare that they have no competing interests.

Received: 19 February 2023 Accepted: 13 June 2023
Published online: 20 July 2023

References

1. Woolston DS, Runyan HL, Andrews RE (1957) An investigation of effects of certain types of structural nonlinearities on wing and control surface flutter. J Aeronaut Sci 24(1):57–63
2. Laurenson RM, Trn RM (1980) Flutter analysis of missile control surfaces containing structural nonlinearities. AIAA J 18(10):1245–1251
3. Lee CL (1986) An iterative procedure for nonlinear flutter analysis. AIAA J 24(5):833–840
4. Yang ZC, Zhao LC (1988) Analysis of limit cycle flutter of an airfoil in incompressible flow. J Sound Vib 123(1):1–13
5. Lee BHK, Tron A (1989) Effects of structural nonlinearities on flutter characteristics of the CF-18 aircraft. J Aircraft 26(8):781–786
6. Chen PC, Sulaeman E, Liu DD et al (2002) Influence of external store aerodynamics on flutter/LCO of a fighter aircraft. In: Proceedings of the 43rd AIAA/ASME/ASCE/AHS/ASC structures, structural dynamics, and materials conference, Denver, 22-25 April 2002.
7. Försching H, Knaack JM (1993) Parametric study of the flutter stability of a semi-rigid 3-D wing-with-engine nacelle model in subsonic flow. J Fluids Struct 7(6):567–593

8. Arizono H, Kheirandish HR, Nakamichi J et al (2008) Transonic flutter simulation for wing-pylon-nacelle configuration using Navier-Stokes equations. In: Proceedings of the 49th AIAA/ASME/ASCE/AHS/ASC structures, structural dynamics, and materials conference, Schaumburg, 7-10 April 2008.
9. Wang L, Wan Z, Wu Q et al (2012) Aeroelastic modeling and analysis of the wing/engine system of a large aircraft. Procedia Eng 31:879–885
10. Neuert N, Dinkler D (2020) Aeroelastic behaviour of a wing with over-the-wing mounted UHBR engine. CEAS Aeronaut J 11(4):1045–1055
11. Yu Q, Lee S, Damodaran M et al (2018) Modelling of flutter characteristics of aircraft wing with pylon-mounted engine nacelle. In: Proceedings of the 31st congress of the international council of the aeronautical sciences, Belo Horzonte, 9-14 September 2018
12. AIAA Applied Aerodynamics Technical Committee (2022) The NASA high lift prediction workshop (From 2010 onwards). https://hiliftpw.larc.nasa.gov/. Accessed 24 April 2023
13. Reymond M (1994) MSC/NASTRAN: quick reference guide, version 68. Los Angeles, The MacNeal-Schwendler Corporation. https://www.mscsoftware.com/product/msc-nastran. Accessed 24 April 2023
14. Albano E, Rodden WP (1969) A doublet-lattice method for calculating lift distributions on oscillating surfaces in subsonic flows. AIAA J 7(2):279–285
15. Liu DD, James DK, Chen PC et al (1991) Further studies of harmonic gradient method for supersonic aeroelastic applications. J Aircraft 28(9):598–605
16. Yu Q, Damodaran M, Khoo BC (2020) Nonlinear airfoil limit cycle analysis using continuation method and filtered impulse function. AIAA J 58(5):1976–1991
17. Yu Q, Damodaran M, Khoo BC (2022) Nonlinear aeroelastic analysis of a multi-element airfoil with free play using continuation method. J Fluids Struct 109(5):103482
18. Trajkovic L, Melville RC, Fang SC (1991) Finding DC operating points of transistor circuits using homotopy methods. In: Proceedings of 1991 IEEE international sympoisum on circuits and systems (ISCAS), Singapore, June 1991. Vol 2. IEEE, pp 758–761
19. Yokokawa Y, Murayama M, Uchida H et al (2010) Aerodynamic influence of a half-span model installation for high-lift configuration experiment. In: Proceedings of the 48th AIAA aerospace sciences meeting including the new horizons forum and aerospace exposition, Orlando, 4-7 Jan 2010
20. Chai S, Crisafulli P, Mason WH (1995) Aircraft center of gravity estimation in conceptual/preliminary design. In: Proceedings of the Aircraft engineering, technology, and operations congress, Los Angeles, 19-21 Sept 1995
21. Komzsik L (1987) The Lanczos method: evolution and application. Society for Industrial and Applied Mathematics, Philadelphia
22. Erickson LL (1990) Panel methods: an introduction. NASA Tech Rep, NASA-TP-2995
23. Ogrodzki J (1994) Circuit simulation methods and algorithms. CRC Press, Boca Raton
24. Meyer EE (1998) Application of a new continuation method to flutter equations. In: Proceedings of the 29th structures, structural dynamics and materials conference, Williamsburg, 18-20 April 1988
25. Rodrigues PJC (1998) Computer-aided analysis of nonlinear microwave circuits. Artech House, Boston
26. ZONA Technology Inc (2017) ZAERO Version 9.3: theoretical manual. https://www.zonatech.com/Documentation/ZAERO%209.3_THEO_Full_Electronic.pdf. Accessed 24 April 2023
27. Tiffany SH, Adams WM Jr (1987) Nonlinear programming extensions to rational function approximations of unsteady aerodynamic forces. In: Proceedings of the 28th structures, structural dynamics and materials conference, Monterey, 6-8 April 1987

Publisher's Note